Electric Power Systems Research 165 (2018) 179–190

Contents lists available at ScienceDirect

Electric Power Systems Research

journal homepage: www.elsevier.com/locate/epsr

Subsynchronous interactions in power networks with multiple DFIG-based wind farms

Gustavo Revel[a,b,*], Diego M. Alonso[a,b]

[a] Instituto de Investigaciones en Ing. Eléctrica (IIIE) Alfredo Desages (UNS-CONICET), Argentina
[b] Dpto. de Ing. Eléctrica y de Computadoras, Universidad Nacional del Sur, San Andrés 800, 8000 Bahía Blanca, Argentina

ARTICLE INFO

Keywords:
Power system dynamics
Subsynchronous interaction
Doubly-fed induction generator
Stability boundary

ABSTRACT

This paper exposes relevant characteristics of the stability boundary associated to subsynchronous control interactions when multiple DFIG-based wind farms are radially connected to a series compensated transmission line. It is shown that the stability boundary is a convex hypersurface in the parameter space defined by the compensation level and the number of wind turbines in service at each wind farm (WF). A comprehensive multi-parameter analysis is carried out, revealing the effect of key parameters such as the location of the WFs and the transmission infrastructure, the gains of the WF controllers, the internal collector impedances and the wind speed on the stability boundary. These results also show that the convexity is a robust property of the boundary. The methodology is applied on a generic power system with two wind farms and on a case study based on a practical scenario, reproducing and explaining behaviors reported previously in practical systems.

1. Introduction

Subsynchronous oscillation (SSO) problems involving series compensated transmission lines and DFIG-based wind farms (WFs) received a great attention in recent years. Important advances have been produced in both analysis (see, for example [1–4]) and mitigation techniques (see, for example [5–8]). The first reported incident occurred in Texas in 2009 [9], and was followed by events in Minnesota [10], Oklahoma [11] and in the north of China [12–14]. The phenomenon has an electromagnetic nature, without involving the mechanical part of the turbine-generator. It is associated to a damping reduction of the subsynchronous electrical mode when, for example, the compensation level of the transmission line increases or when the wind speed diminishes. The subsynchronous mode and the related dynamical behavior are also affected by the number of DFIG wind turbines in operation, the impedance of the internal WF grid (collectors and transmission lines), and the tuning of the controllers, among others parameters. The problem has reminiscences to the induction generator effect (IGE) arising in conventional synchronous generators. Nevertheless, since it not only involves the DFIG but also its power converters, it has been classified as a subsynchronous control interaction (SSCI) [9,1]. A peculiar feature of the SSCI is that the frequency of the resulting SSO is not fixed, and depends on the grid and WF parameters (including the tuning of the DFIG controllers). In addition, since the mechanical part of the turbine-generator is not engaged, the oscillations emerge and grow relatively fast.

In regions with extensive areas with high-quality wind resources and relatively low consumptions, such as the south of Argentina (Patagonia) [15–17] and the north of China [12], several WFs are connected through dedicated transmission lines to a common point on the main corridors, exporting the wind generated power to distant load centers. The main corridors often have series capacitive compensation and thus, these scenarios are prone to undergo SSCI problems, such as the ones observed in several WFs located in the Hebei Province in the north of China [12–14]. In this regard, Wu et al. [13] evaluated the impact of two and five practical WFs connected to a common point in the power grid, concluding that SSCI events can arise, due to a contingency or a reduction in the wind speed, even when the compensation level is relatively low. They also pointed out that the frequency varies during the incident due to the number of machines in service, and that the rotor side converter (RSC) of the DFIG plays an important role since it modifies the equivalent impedance of the machine. Xie et al. [14] corroborated the theoretical results by analyzing field data corresponding to 58 incidents occurred in the Guyuan power system located in Hebei, China.

In practical systems the number of wind turbines in service plays an important role in the oscillatory behavior associated to SSCI [14]. This problem can be further interpreted by examining the structure of the

* Corresponding author at: Instituto de Investigaciones en Ing. Eléctrica (IIIE) Alfredo Desages (UNS-CONICET), Argentina
E-mail addresses: grevel@uns.edu.ar (G. Revel), dalonso@uns.edu.ar (D.M. Alonso).

https://doi.org/10.1016/j.epsr.2018.09.009
Received 6 January 2018; Received in revised form 14 July 2018; Accepted 9 September 2018
Available online 24 September 2018

critical conditions associated to the SSCI phenomenon, *i.e.* exposing the stability boundary in the parameter space defined by the compensation level and the number of wind turbines in operation (available power) at each WF. In this paper, generic properties of the stability boundary are derived using tools from bifurcation theory. Since the mechanism leading to the SSCI phenomenon is a Hopf bifurcation [18], the mathematical properties of this bifurcation are used to characterize the stability boundary in the considered parameter space. The main contribution consists in revealing that the stability boundary is a *convex hypersurface*.[1] This property implies that the minimum or critical compensation level is unique, and for compensation levels higher than this critical value, the stability boundary is a closed convex region restricting the admissible WFs powers to values outside this region. In other words, the stability depends not only on the cumulative number of wind turbines in operation but also on its geographical distribution. In addition, changes in the number of in-service wind turbines in the WFs, can drive the system from a stable operating condition to another stable condition, but depending on the sequence followed when connecting or reconnecting the turbines, the system can exhibit SSCI phenomena during the transition. This reveals that the combined characteristics of the WFs are decisive in the stability of the system. This feature is generic since the Hopf bifurcation is also generic. Furthermore, the characteristics of this boundary are disclosed numerically, including the effects of the location of the WFs and the transmission infrastructure connecting them to the bulk power system, the gains of the WF controllers, the internal collector impedances and the wind speed. The results are illustrated with time domain simulations, considering two generic WFs and a case study based on a practical scenario. The convexity of the stability boundary paves the way to implement minimum search algorithms to distinguish the worst case scenario that can be used to detect the minimum compensation level admissible for a given system. The paper is organized as follows. In Section 2, a network model suitable for SSCI studies is introduced. Preliminary concepts regarding the SSCI phenomenon and the methodology used in this paper are described in Section 3. The main features of the SSCI considering one WF is presented in Section 4. Section 5 analyzes the scenario with two WFs, and the results are extended to a case study involving several WFs in Section 6. Finally, the conclusions are given in Section 7.

2. Power system model for SSCI analysis

To analyze the SSCI phenomenon in a multiple WFs scenario, a power system with the structure depicted schematically in Fig. 1 is considered. It consists in a set of WFs transferring the generated power through dedicated lines, generally, with different lengths, parameters, voltage levels, etc. The power is collected at the point of interconnection (POI) and transmitted to the bulk system through a series compensated line. This radial scenario retains the main features involved in the SSCI and, simultaneously, preserves the features of individual WFs (or a group of nearby WFs), such as the installed power, location and line impedances, controller gains, among others, that are essential for the analysis. Similar representations were used in [12,13,19] to describe SSO incidents in WFs integrated to the power grid in the north of China.

2.1. Wind farm representation

In general, the turbines of a large scale WF are arranged in several strings or collectors, connecting a relatively small number of turbines to the WF substation. A practical method for deriving a simplified model consists in representing each collector by a single wind turbine with an equivalent power S_C, an equivalent pad-mounted transformer X_{TC}, and an equivalent internal network impedance Z_C (see for example [20]). For simplicity, in this paper, it is assumed that the n_C collectors are identical and that all the wind turbines operate at the same point. Therefore, the WF aggregated model results in a wind turbine with power $S_{wf} = n_C S_C$, a transformer with reactance $X_{Twf} = X_{TC}/n_C = X_{TC}S_C/S_{wf}$ and an internal network impedance $Z_{wf} = Z_C/n_C = Z_C S_C/S_{wf}$, as depicted schematically in Fig. 2 (inside the dashed line rectangle).

2.2. Power grid representation

The equivalent WF is connected to the POI through a substation (with reactance X_{TS}) and a dedicated line (with impedance Z_l). In the considered case, the voltage levels are: 0.69 kV for the DFIG wind turbine output, 33 kV for the WF internal network and 132 kV for the WF dedicated line. A 132/500 kV transformer (with reactance X_{TL}) steps-up the voltage to the bulk transmission level. The main corridor is represented by the impedance $Z_L = R_L + jX_L$ and is compensated with a fixed series capacitor bank with reactance X_C. The compensation level μ, with $0 < \mu < 1$, is defined as

$$\mu = \frac{X_C}{X_L}, \tag{1}$$

i.e. only the reactance of the main corridor is compensated. The bulk power system is modeled as an equivalent 500 kV/50 Hz power source with a short circuit power S_{SC} and impedance Z_{SC}.

2.3. Power system model

The system is modeled by a set of ordinary differential equations, including the equivalent wind turbine dynamics with the corresponding control loops in local *d-q* coordinates, and the transmission lines and the bulk system in the synchronous *d-q* reference frame. The details of the implemented models and the values of the parameters are described in Appendix A. The resulting power system model can be generically expressed as

$$\dot{x} = f(x, \alpha), \tag{2}$$

where $f: \mathbb{R}^n \times \mathbb{R}^m \to \mathbb{R}^n$ is a smooth vector field, depending on the state variables $x \in \mathbb{R}^n$ and on the subset of parameters under consideration $\alpha \in \mathbb{R}^m$.

3. Preliminaries: SSCI phenomenon and the Hopf bifurcation mechanism

The SSCI phenomenon in DFIG-based WFs is associated to the damping reduction of the subsynchronous electrical mode introduced by the capacitive series compensation of the transmission line. Some key parameters are the compensation level (μ), the wind speed (v_w), the number of wind turbines in operation in the WF (represented by their rated powers S_{wf}) and the tuning of the controllers. The behavior of the relevant eigenvalues when these parameters vary is described in detail in [18] for a radial system with one WF. In particular, an increase of the compensation level or a decrease of the wind speed has a negative effect on the damping of the subsynchronous mode. Thus, poorly damped SSO can arise, resulting in excessive currents that affect the series capacitors and WFs equipment. Ultimately, when the subsynchronous mode crosses the imaginary axis, the operating point becomes unstable due to a Hopf bifurcation and a sustained SSO takes place. Therefore, the underlying mechanism behind the SSCI phenomenon is a Hopf bifurcation. The locus of this bifurcation in the parameter space defines the stability boundary, *i.e.* the parameter values for which a sustained SSO appears. In addition, the proximity to the curve alerts for a poorly damped subsynchronous mode. Since the Hopf bifurcation plays a key role in determining the stability of the system related to the SSCI

[1] A $(m-1)$–dimensional manifold in the considered m–dimensional parameter space.

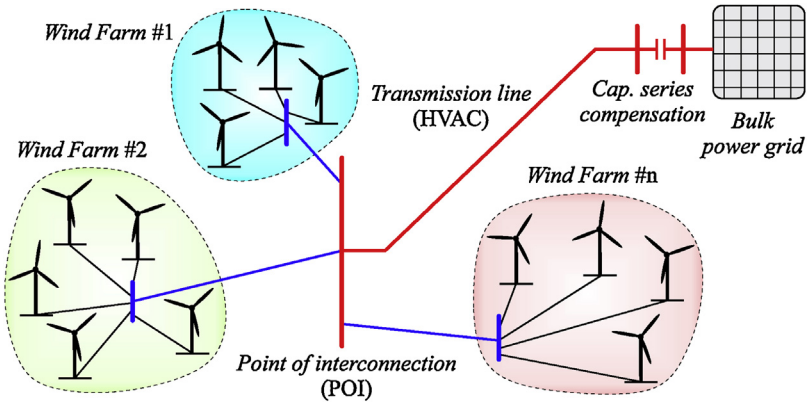

Fig. 1. Schematic portrait of the radial topology considered in this paper.

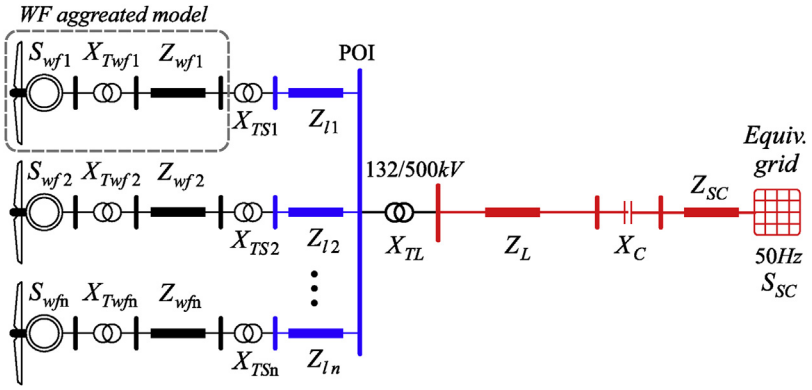

Fig. 2. Radial corridor with n WFs represented by the corresponding aggregated model (box).

phenomenon, the main concepts regarding the defining conditions and the method used for the continuation of bifurcation points are introduced next.

3.1. Detection and continuation of Hopf bifurcations

Consider the power system (2) and, without loss of generality, suppose that the dynamics is analyzed in terms of one parameter of the system, *i.e.* $\alpha \in \mathbb{R}^1$ (the subset of parameters that can vary has dimension $m = 1$). The operating points of (2) when α is varied are obtained by solving the equilibrium equation $f(x, \alpha) = 0$, which defines a curve in $\mathbb{R}^n \times \mathbb{R}^1$. This curve is a one-dimensional manifold M that can be computed by the elementary approach consisting in fixing successive values of α and solving the equilibrium equation with standard numerical methods for nonlinear equations. Alternatively, the curve can be computed using the so called *continuation method*. In this context the manifold M is defined by the set of equations $F(y) = 0$, with $y = (x, \alpha) \in \mathbb{R}^n \times \mathbb{R}^1$ and $F: \mathbb{R}^n \times \mathbb{R}^1 \to \mathbb{R}^n$. The method computes a sequence of points $\{y^1, y^2, \dots\}$ that approximates M with the desired tolerance by means of an iterative prediction-correction approach. The successive points are predicted using the vector tangent to the curve, and the resulting values (expectedly close to M) are corrected by Newton iterations. The step size used to update the parameter value is adapted when convergence is not achieved.

An equilibrium point $x = x^*$ of (2) undergoes a Hopf bifurcation if for some $\alpha = \alpha^*$ such that $f(x^*, \alpha^*) = 0$, the Jacobian matrix $D_x f(x^*, \alpha^*)$ has a pair of eigenvalues on the imaginary axis, namely $\lambda_{1,2}(\alpha) = \pm i\omega_0$ with $\omega_0 > 0$, and the following conditions are satisfied:

i) The pair of eigenvalues $\lambda_{1,2}(\alpha)$ crosses the imaginary axis transversally, *i.e.* $d\mathrm{Re}\lambda_{1,2}(\alpha)/d\alpha|_{\alpha=\alpha^*} \neq 0$.
ii) The first Lyapunov coefficient is $l_1(\alpha^*) \neq 0$ (non-degeneracy).[2]

The first Lyapunov coefficient, defines the stability of the emerging limit cycle. Thus, if the equilibrium point is unstable for $\alpha > \alpha^*$ and $l_1(\alpha^*) < 0$, a stable limit cycle with frequency ω_0 and amplitude $\sqrt{\alpha - \alpha^*}$ arises for $\alpha > \alpha^*$.

During the equilibrium point continuation, the Hopf bifurcation can be detected by computing the scalar test function $\Psi_H(y) = \prod_{i>j} (\lambda_i(y) + \lambda_j(y))$, which is zero when the eigenvalues are on the imaginary axis. A procedure for computing this scalar function that avoids the explicit calculation of the eigenvalues can be consulted in [21,Sec. 10.2.2]. The Hopf bifurcation is a codimension one phenomenon since it requires the tuning of a single parameter of the system. Once a Hopf bifurcation point is detected, it can be continued in the parameter space by considering variations of a second parameter, hence $\alpha \in \mathbb{R}^2$. In this case the same tools used in the equilibrium continuation can be applied to solve simultaneously the equilibrium equation $F(y) = 0$, with $y = (x, \alpha) \in \mathbb{R}^{n+2}$ and $F: \mathbb{R}^n \times \mathbb{R}^2 \to \mathbb{R}^n$, and the test function $\Psi_H(y) = 0$, *i.e.* by solving the system

$$\begin{cases} F(y) = 0, \\ \Psi_H(y) = 0, \end{cases} \tag{3}$$

numerically, with an iterative prediction-correction algorithm that exploits the information given by the tangent vector. Since the Hopf bifurcation is a codimension one phenomenon, the difference between the dimension of the parameter space and the one of the bifurcation boundary is one (for the m–dimensional parameter space, the bifurcation boundary is a $(m - 1)$–dimensional manifold).

Usually, the Hopf bifurcation (as well as other bifurcations) are detected and continued in the parameter space using standard numerical continuation packages. This is particularly useful when variation of

[2] A procedure for computing l_1 can be consulted in [21,Sec. 5.4.1].

Table 1
Electric network parameters in p.u. for a base of 100 MVA and the corresponding nominal transmission line voltage (500/132/33 kV).

HVAC transmission system (500 kV)		
Short-circuit power	S_{SC}	180 p.u.
Short-circuit impedance	Z_{SC}	$(0.553 + j5.53) \times 10^{-3}$ p.u.
Line impedance (354 km)	Z_L	$(1.375 + j16.920) \times 10^{-3}$ p.u.
Transformer 132/500 kV	X_{TL}	$j0.027592$ p.u.
WF transmission system (132 kV)		
Single line rated power	S_l	1.4 p.u.
Line impedance (10 km)	Z_l	$(8.07 + j22.77) \times 10^{-3}$ p.u.
Transformer 33/132 kV	X_{TS}	$j0.0954$ p.u.
WF collectors (33 kV)		
Equiv. machine power	S_C	0.5 p.u.
Equiv. collector impedance	Z_C	$(5.20 + j5.61) \times 10^{-3}$ p.u.
Equiv. transf. 0.69/33 kV	X_{TC}	$j0.1739$ p.u.

several parameters are considered. In this paper, the package MatCont [22] is used.

4. Analysis of SSCI and stability boundary in a single WF

In order to review the main features related to SSCI, and to begin the analysis of the stability boundary, a system consisting in a single WF radially connected to the bulk power grid (Fig. 2 with $n = 1$) is considered. The parameter values, obtained from a portion of the Argentinean power system, are included in Table 1 (the base power is 100 MVA). In this section, the length of the 132 kV dedicated line is $l = 10$ km and the wind speed is fixed at $v_w = 5.5$ m/s (close to the lowest value and thus a worst case scenario). The stability boundary associated to the SSCI (Hopf bifurcation curve) is investigated in terms of the rated power of the wind turbines in operation (S_{wf}) and the compensation level (μ). The parameter S_{wf} is varied continuously instead of using discrete values $n_C S_C$. To show the effect of the line impedance, a different number (n_l) of parallel 132 kV lines is considered. Each line has a maximum rated power of $S_l = 1.4$ p.u., limiting the admissible WF power to $S_{wf} < 1.4 \times n_l$ p.u. The results for $n_l = 2$, 3 and 4, are depicted in Fig. 3. In each case, the corresponding curve, delimits the stable region (below) and the unstable one (above). The shape of the curve is the same for all the scenarios, but the stability boundary is shifted-down, reducing the stable region, as the number of lines is increased (the equivalent line impedance diminishes).

The convexity of the stability boundary curve has an important effect on the behavior related to SSCI that is exposed when the number of turbines in operation changes. For example, consider a stressed scenario with $S_{wf} = 5$ p.u. and $n_l = 4$, *i.e.* close to the maximum rating ($1.4 \times 4 = 5.6$ p.u.), for a compensation level $\mu = 0.65$. According to Fig. 3, the operating condition (blue triangle) is stable since it is located below the blue curve. The tripping of wind turbines moves the operating condition to the left, reducing the stability margin (diminishing the damping of the subsynchronous mode). When the apparent power of the WF is reduced in at least 80 MVA due to wind turbine disconnections, the stability boundary curve is crossed (at $S_{wf} \simeq 4.2$ p.u.) and a sustained SSO occurs for $1.5 < S_{wf} < 4.2$ (*c.f.* the blue triangle at $S_{wf} = 2.5$ p.u.). The stable operation is recovered when the number of tripped turbines increases and $S_{wf} < 1.5$ p.u. (*c.f.* blue triangle at $S_{wf} = 0.5$ p.u.).

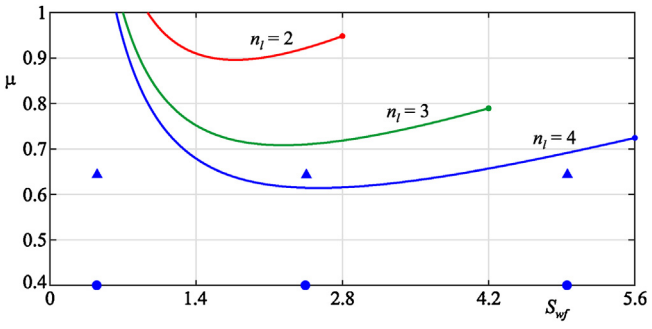

Fig. 3. Stability boundary (Hopf bifurcation curve) associated to SSCI considering a different number of 132 KV transmission lines, each one with a maximum capacity of 1.4 p.u. (140 MVA). (For interpretation of the references to color in the text, the reader is referred to the web version of this article.)

The related dynamical behavior is illustrated by a numerical simulation performing a small voltage sag at the equivalent grid bus. The resulting active power at the POI is shown in Fig. 4a (the corresponding values of S_{wf} are denoted by the blue triangles in Fig. 3). The simulation starts with a WF in-service power $S_{wf} = 5$ p.u., *i.e.* a stable operating point according to Fig. 3. The perturbation is introduced at $t = 0.1$ s, and the system responds with a poorly damped oscillation (reduced stability margin). At $t = 1.5$ s the tripping of wind turbines reduces the WF power to $S_{wf} = 2.5$ p.u., crossing the stability boundary curve and triggering a sustained oscillation. The stability is recovered when a second pack of wind turbines (2 p.u.) is disconnected at $t = 3$ s, reducing the power to $S_{wf} = 0.5$ p.u. and placing the operating point at the left of the stability boundary (see Fig. 3). A similar behavior on a practical WF, triggered by a variation of the wind speed, was described in [12] using eigenvalue analysis. To complete the description of the dynamics, Fig. 4b shows the simulation results obtained for $\mu = 0.4$ (*c.f.* blue dots in Fig. 3), where the improvement on the stability margin due to the reduction of the compensation level is evident. In both cases the frequency of the oscillation is approximately 10 Hz.

The stability boundary can also be analyzed in terms of the grid stiffness. Towards this end, the boundary is computed varying the short circuit power S_{SC} for a fixed number of transmission lines ($n_l = 4$) and a fixed WF operating power ($S_{wf} = 2.5$ p.u.). The result is depicted in Fig. 5, where the operating conditions for $\mu = 0.65$ (triangle marker) and $\mu = 0.4$ (circle marker) are denoted (*c.f.* Fig. 3). It is worth noticing that the problem aggravates as the short circuit power at the equivalent grid increases. This is explained by the reduction of the short circuit impedance and the consequent reduction of the resistance.

These results reveal that the Hopf bifurcation plays a decisive role in the SSCI phenomenon and that the complete stability boundary should be analyzed to avoid SSCI problems. As will be demonstrated in the following, this conclusion can be extended to the multiple WFs scenario.

5. Analysis of SSCI and stability boundary in a two WFs scenario

To begin the analysis of the stability boundary in the multiple WF scenario, the radial system in Fig. 2 with two WFs, namely WF_1 and WF_2, is considered. The power on each WF is limited to $S_{wf} < 5.6$ p.u. (four parallel 132 kV lines are implemented).

The first analysis is performed with identical WFs, operating at the same conditions ($v_w = 5.5$ m/s), and transmission lines of the same lengths ($l_1 = l_2 = 10$ km). The stability boundary in terms of S_{wf1} and S_{wf2}, associated to the number of wind turbines in service at each WF, and the compensation level μ is depicted in Fig. 6a (the color indicates the value of μ). The surface is developed by performing and assembling two-dimensional continuations of the SSCI condition (Hopf bifurcation), on a sufficient large number of slices of the 3-D parameter space defined by planes of constant power ratios $K_{SW} = S_{wf2}/S_{wf1}$. The locus of the Hopf bifurcation on each slice is a curve similar to the ones depicted in Fig. 3. Since the transmission lines have the same length and both WFs are identical and operate at the same condition, WF_1 and WF_2 are indistinguishable and the surface is symmetric with respect to the slice $K_{SW} = 1$, *i.e.* $S_{wf1} = S_{wf2}$ (denoted by the black dashed line on the surface in Fig. 6a). The stable operating region is located below the surface and the damping of the subsynchronous mode is reduced when the operating point approaches this boundary.

The combined effect of S_{wf1}, S_{wf2} and μ is better interpreted focusing

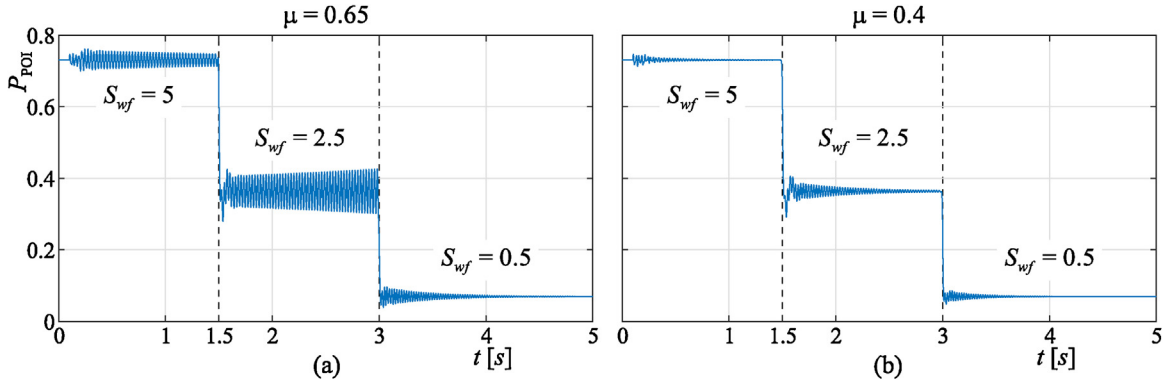

Fig. 4. Simulation results with a single WF connected to the main corridor by means of four 132 kV lines ($n_l = 4$). A small voltage sag is applied at the equivalent grid bus at $t = 0.1$ s. Wind turbines are disconnected at $t = 1.5$ s and $t = 3$ s. (a) $\mu = 0.65$; (b) $\mu = 0.4$.

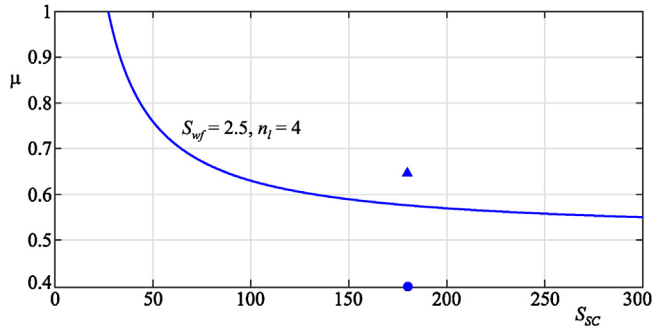

Fig. 5. Stability boundary (Hopf bifurcation curve) associated to SSCI as the grid stiffness is varied ($S_{wf} = 2.5$ p.u. and $n_l = 4$).

the attention on the top view of the surface shown in Fig. 6b. Given a compensation level $\mu > \mu_{min} = 0.473$, the stability boundary, *i.e.* where the Hopf bifurcation occurs and the SSCI arises, is given by a closed curve or contour that restricts the operating region. For example, for $\mu = 0.5$, the feasible region is limited to power combinations near the axes, and if the power in one of the WFs does not exceed approximately 0.75 p.u., the second WF can adopt any value provided that the maximum power of the line is not exceeded. Notice that there exist other stable points outside this contour, for example $S_{wf1} = S_{wf2} = 3$ p.u., but the operation in this region is hazardous since a reduction in the number of connected wind turbines on the WFs, can drive the system to an unstable condition (inside the level curve). When the compensation level decreases, the boundary curve shrinks until it collapses at $\mu = \mu_{min}$ (near the point $S_{wf1} = S_{wf2} \simeq 1.65$ p.u.), and for $\mu < \mu_{min}$, a SSCI cannot occur for any combination of S_{wf1} and S_{wf2}. On the other hand, when the compensation level increases, the contour grows, restricting the stable operating region, *i.e.* restricting the admissible power combinations. For example, for $\mu = 0.6$, the feasible operating conditions are limited to small WF powers (lower left corner). Operating points with one or both WFs near the maximum value (5 p.u.), are also stable, but applies the same remark given previously for $\mu = 0.5$ (when $S_{wf1} = S_{wf2} = 3$ p.u.).

Notice that the boundary surface is convex, the contours arise at $K_{SW} = 1$ for $\mu = \mu_{min}$, and are symmetric with respect to this power ratio. In other words, for $\mu > \mu_{min}$, the scenario is prone to exhibit a SSCI when the powers at the WFs are similar, and a potential SSCI problem can be overlooked when the imbalance between the in-service power in WF_1 and WF_2 increases. Therefore, when the WFs are identical and the lines have the same lengths, the power ratio $K_{SW} = 1$ is a worst case scenario and can be used to determine the risk of a SSCI. Thus, given a compensation level, if the system is stable for all the power combinations satisfying $S_{wf1} = S_{wf2}$, the system cannot undergo a SSCI for any other power ratio.

Although the particular scenario of identical WFs and lines could be studied by means of an equivalent WF (aggregated model), the results would coincide with the ones corresponding to $K_{SW} = 1$, but hiding the scenarios of WFs with different powers. As will be shown in the following, this kind of analysis is very useful to understand the behavior related to SSCI when the WFs or their transmission lines are different.

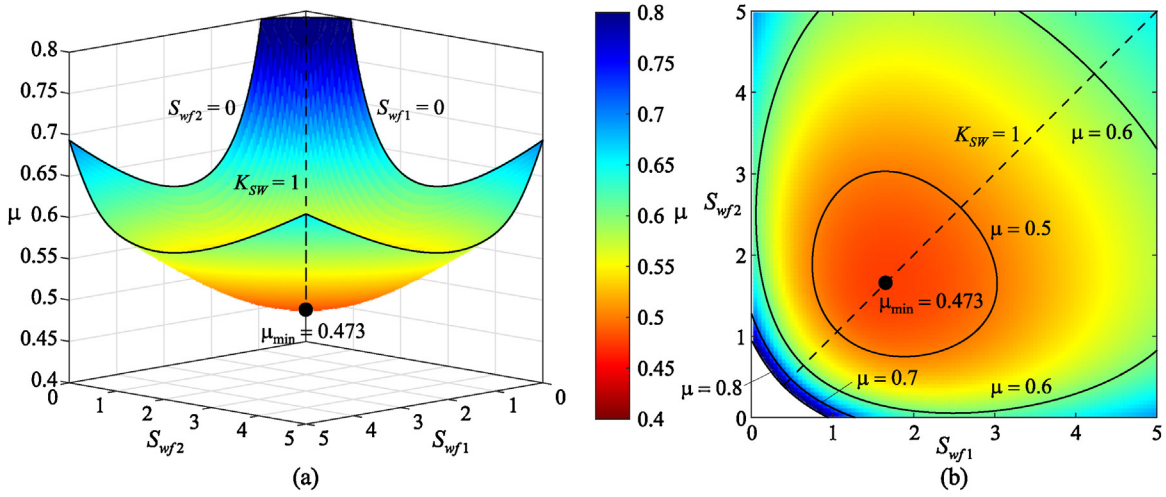

Fig. 6. Stability boundary for two WFs with lines of equal lengths ($l_1 = l_2 = 10$ km). (a) 3-D boundary; (b) Level curves for μ fixed.

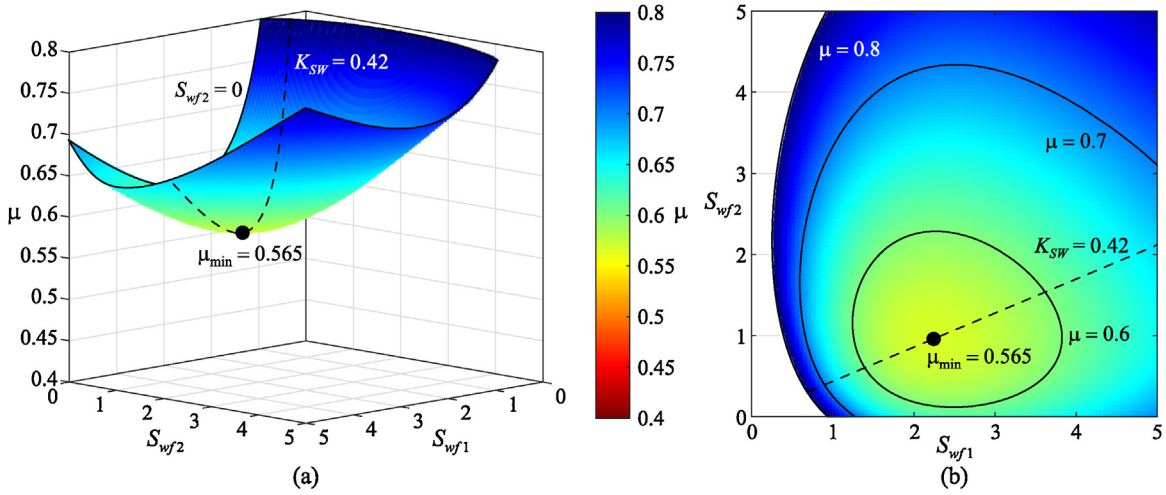

Fig. 7. Effect of the wind speed on the stability boundary (v_w = 5 m/s at WF_1 and v_w = 8 m/s at WF_2) for $l_1 = l_2 = 10$ km. (a) 3-D boundary; (b) Level curves for μ fixed.

5.1. Effect of the WFs wind speed

It is well known that the SSCI is prone to arise in low wind speed conditions. Thus, an increment in the wind speed should improve the stability boundary. This is revealed in Fig. 7, where the wind speed in WF_2 is increased to 8 m/s (the wind speed in WF_1 remains at v_w = 5.5 m/s and $l_1 = l_2 = 10$ km). By comparing this scenario with the one in Fig. 6, the overall situation improves, resulting in $\mu_{min} = 0.565$. Since the improvement in the wind condition was introduced in WF_2, the worst case power ratio is skewed towards WF_1 as shown in Fig. 7b. Now, the contours arise at $S_{wf1} \simeq 2.25$ p.u. and $S_{wf2} \simeq 0.95$ p.u., *i.e.* for $K_{sw} = S_{wf2}/S_{wf1} = 0.42$. Moreover, the convexity of the stability boundary is preserved.

5.2. Effect of the WFs transmission lines

When both lines are shortened (maintaining the same lengths), the stability boundary surface is displaced towards lower compensation levels, preserving the symmetry with respect to $K_{SW} = 1$. The minimum compensation level μ_{min} decreases and the contours grow. On the contrary, when longer lines are considered, the surface is displaced towards higher compensation levels and the boundary contours shrink.

When the WFs transmission lines have different lengths, the symmetry with respect to $K_{SW} = 1$ is destroyed, as displayed in Fig. 8a for $l_1 = 5$ km and $l_2 = 15$ km. Comparing this surface with Fig. 6a (obtained for $l_1 = l_2 = 10$ km), shows that the reduction of l_1 pulls-down the edge $S_{wf2} = 0$, deteriorating the scenarios in which the power is concentrated at WF_1. On the other hand, the increment in l_2 pulls-up the border $S_{wf1} = 0$, improving the cases with a power concentration in WF_2. This is noticed in Fig. 8b, where the level curves are skewed towards the horizontal axis ($S_{wf2} = 0$). In this case, $\mu_{min} = 0.453$ and the level curves are enlarged with respect to the base case $l_1 = l_2 = 10$ km. For example, for $\mu = 0.5$, the level curve reduces the admissible powers in WF_1 to small values, and if $S_{wf1} < 1$ no restrictions apply to the admissible power in WF_2. Greater values of S_{wf1} could be admitted if the power in WF_2 is restricted severely. Notice that for $S_{wf2} > 2.75$ p.u. approximately, no restriction apply to S_{wf1}, but a contingency originating the trip of wind turbines in WF_2 with $S_{wf1} > 1$, will drive the system to the unstable operating region, *i.e.* inside the corresponding stability boundary (Fig. 8b). To illustrate this situation, suppose a stable scenario with $S_{wf1} = 2$ p.u., $S_{wf2} = 3$ p.u. and $\mu = 0.5$. The trip of wind turbines in WF_1 does not jeopardize the stability, but the trip of a quarter of the turbines in WF_2, reduces the power to $S_{wf2} = 2.25$ p.u., resulting an operating point inside the contour and triggering a SSCI.

It is worth mentioning that the convexity of the stability boundary surface is preserved and $\mu_{min} = 0.453$ is achieved at $S_{wf1} \simeq 2.44$ p.u. and $S_{wf2} \simeq 1$ p.u., *i.e.* a slice with $K_{SW} \simeq 0.41$. Therefore, in this case, the power ratio $K_{SW} \simeq 0.41$ can be selected as the worst case scenario and

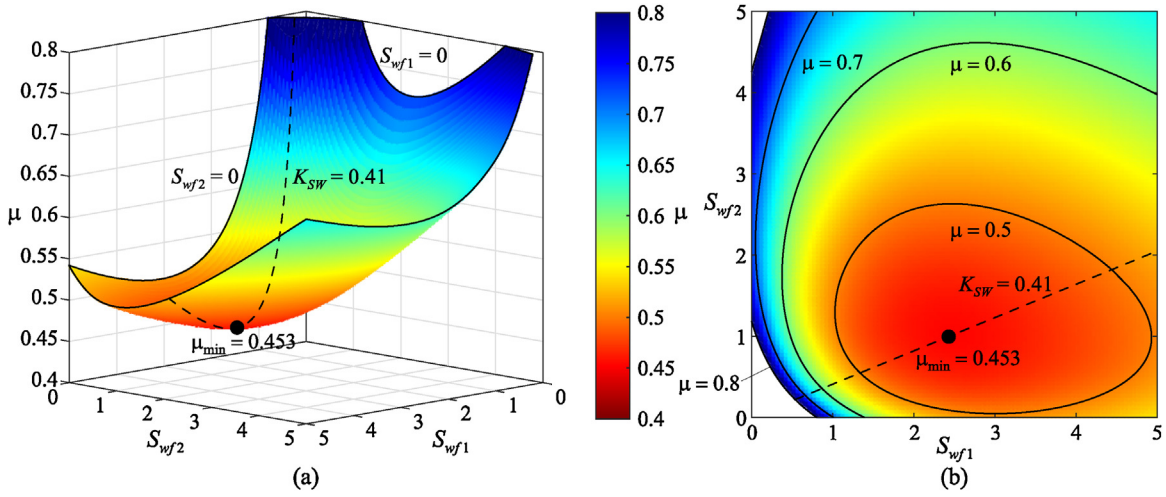

Fig. 8. Stability boundary for two WFs with lines of different lengths (l_1 = 5 km and l_2 = 15 km). (a) 3-D boundary; (b) Level curves for fixed μ.

can be used to determine the risk of SSCI. In general, a reduction of the line impedance of one of the WFs or the increment in the other, tilts the worst case power ratio to the WF where the impedance is lowered, or opposite to the one where the impedance is increased.

5.3. Effect of the WFs collector impedances

A variation in the internal configuration of the WF can be represented as a variation of the equivalent collector impedance Z_{wf}. The effect on the stability boundary is similar to the one illustrated in Fig. 8 with variations in the impedance of the line, *i.e.* increasing (decreasing) collector impedance of one WF improves (deteriorates) the stability region in all the cases.

5.4. Effect of the WFs controller gains (RSC inner loop)

The effect of the WFs controllers on the SSCI is carried out assuming WFs transmission lines of equal lengths ($l_1 = l_2 = 10$ km) and varying the gain K_{r2} of the internal PI loop of the RSC in WF_2 (the controller is implemented as $PI(s) = K_{r2}[1 + (T_{ir2}s)^{-1}]$). The results for $K_{r2} = 0.6\,K_{r2}^*$ and $K_{r2} = 1.4\,K_{r2}^*$ ($K_{r2}^* = 0.025$ is the nominal value used in the base scenario of Fig. 6) are presented in Fig. 9a and b, respectively. For brevity, the 3D stability boundaries are omitted, and only the 2D top views are shown.

Since the modifications are introduced only in WF_2, the edge of the boundary stability surface corresponding to $S_{wf2} = 0$ does not change, but the one corresponding to $S_{wf1} = 0$, is pulled-up when K_r is diminished and pulled-down when it is increased. Roughly speaking, the net effect on the stability boundary is similar to a variation of the length of the WF_2 transmission line. Therefore, the stability margin is improved when the gain is decreased, as is indicated by Fig. 9a (c.f. Fig. 6b). The minimum compensation value is $\mu_{min} = 0.545$ for $S_{wf1} \simeq 2.11$ p.u. and $S_{wf2} \simeq 1.20$ p.u. Thus, the level curve for $\mu = 0.5$ does not appear, and the one for $\mu = 0.6$ is notably reduced. Since the improvement is introduced in WF_2, the level curves and the worst case scenarios are tilted towards the S_{wf1} axis ($K_{SW} \simeq 0.57$), as expected. On the other hand, when the gain is increased, the stability margin is degraded with respect to the nominal case, as is clearly seen by comparing Fig. 9b with Fig. 6b. In this case $\mu_{min} = 0.403$, and the operating region is restricted severely for $\mu > 0.5$. In addition, the worst case scenario arises at $S_{wf1} \simeq 2$ p.u. and $S_{wf2} \simeq 1.24$ p.u., *i.e.* $K_{SW} \simeq 1.62$.

These results, agree with the ones considering a single WF (see, for example, [18]) in the sense that a reduction (increment) of the bandwidth improves (degrades) the stability margin. Furthermore, the modification of the gain introduced in one WF affects the stability boundary of the entire system.

6. Case study

In order to describe the relevant features of the stability boundary on a practical power system, a case study derived from a future scenario analyzed by the Argentinean TSO is considered. The system is shown in Fig. 10 and consists in three large scale DFIG-based WFs connected to the POI (node 10) by means of transmission lines of different lengths and voltage levels. The WFs PM (Puerto Madryn), LB (Loma Blanca) and LD (La Deseada) are represented by the corresponding aggregated model, with different mechanical and electrical parameters (extracted from [23,5,18], respectively, and included in Table A.3).

The wind power is exported to the bulk system using a 500 kV radial corridor (354 km from node 10 to 1008). The impedance of this corridor (Z_L) and the equivalent short-circuit impedance (Z_{SC}) and power (S_{SC}) at node 1008 are listed in Table 1. The parameters of the transmission lines and transformers connecting the WFs to the POI (node 10) as well as the WFs modules, obtained from the TSO guide, are included in Table 2. The impedance of the line (Z_l) connecting the WF PM (node 245) to the POI comprises three 132 kV parallel lines (each one with the parameters of Table 2) and the 132/500 kV transformer. Analogously, the WF LB (node 275) includes two 132 kV lines and the corresponding transformer, and LD is connected directly to the 500 kV system, by means of a radial corridor joining the buses 53, 12 and 10. Although LD is 567.3 km away from the POI, the electrical distance is similar to the line of PM (three parallel 132 kV lines of 15 km). On the other hand, LB is 42.6 km away from the POI, but the electrical distance is much longer than the ones of PM and LD.

The stability boundary associated to the SSCI phenomenon as a function of the WFs powers and the compensation level is four dimensional. Slices of this hypersurface in the plane S_{wfLD} and S_{wfPM}, and the compensation level μ, for three different values of S_{wfLB} are shown in Fig. 11. The convexity of the stability boundary becomes evident when comparing these diagrams. For $S_{wfLB} = 0$ (Fig. 11a), the risk of a SSCI arises when $\mu > 0.482$, restricting the stable operating region as depicted by the level curves for $\mu = 0.5, \ldots, 0.8$. Increasing S_{wfLB}, the level curves grow and the SSCI can arise for lower values of μ. The largest size of the level curves and the minimum value of the compensation level $\mu = \mu_{min} = 0.457$ is obtained for $S_{wfLB} \simeq 0.5$ p.u. (Fig. 11b). For $S_{wfLB} > 0.5$ p.u., the level curves shrink and the SSCI is triggered for larger values of μ, as shown in Fig. 11c for $S_{wfLB} = 1.5$ p.u.

The convexity of the stability boundary ensures that for $\mu < \mu_{min}$, the system is stable, *i.e.* a SSCI cannot arise, for any combination of WFs powers. In addition, for $\mu = \mu_{min}$ the critical operating point occurs for

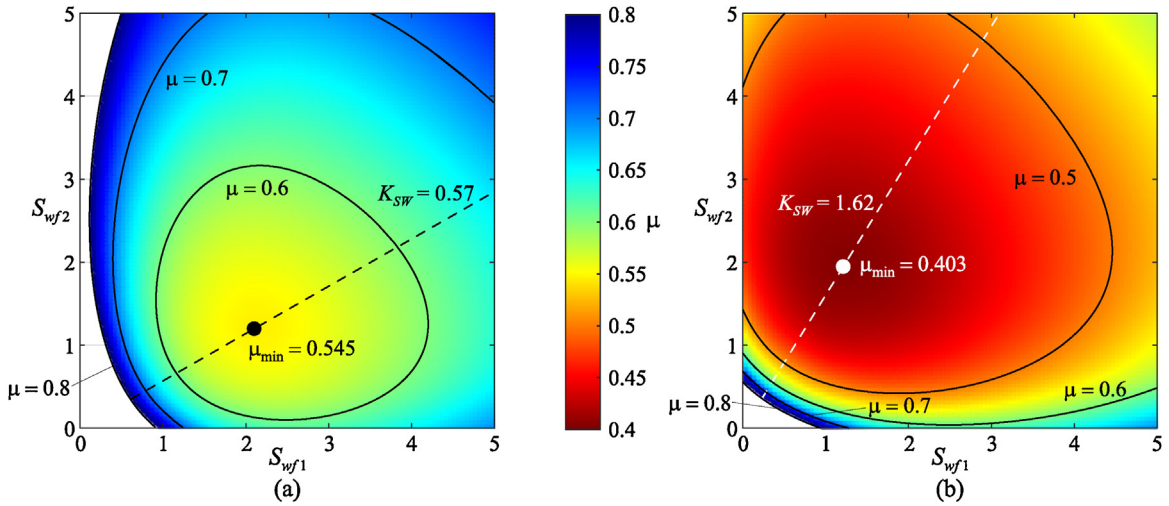

Fig. 9. Effect of the gain K_{r2} (WF_2) on the stability boundary for $l_1 = l_2 = 10$ km. (a) $K_{r2} = 0.6\,K_{r2}^*$; (b) $K_{r2} = 1.4\,K_{r2}^*$.

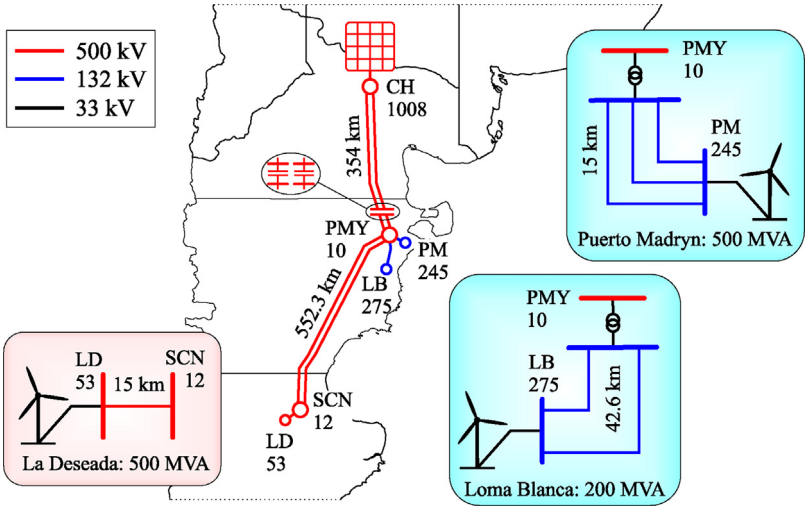

Fig. 10. Schematic diagram of a portion of the Argentinean power system with multiple WFs used to study the SSCI on a practical scenario.

Table 2
Network parameters of the Argentinean case study (Fig. 10).

Transmission lines from each WFs to the POI (node 10)

WF	Line	R	L	B	X_T
PM	10-245	0.00835	0.03220	0.0076	0.05183
LB	10-275	0.02291	0.09327	0.0235	0.07174
LD	10-12	0.00401	0.05098	6.6527	–
	12-53	0.00014	0.00146	0.1754	–

WF internal network

Module	Node	R	L	X_{Twf}	X_{TS}
PM	245	0.00520	0.00560	0.1739	0.2
LB	275	0.00861	0.01949	0.1739	0.2
LD	53	0.01063	0.01124	0.0722	0.084

$S_{wf\mathrm{LD}}$ = 2 p.u., $S_{wf\mathrm{PM}}$ = 2.3 p.u. and $S_{wf\mathrm{LB}}$ = 0.5 p.u. Therefore, defining the power ratios $K_{SW1} = S_{wf\mathrm{PM}}/S_{wf\mathrm{LD}}$ and $K_{SW2} = S_{wf\mathrm{LB}}/S_{wf\mathrm{LD}}$, the worst case scenario results in the direction defined by K_{SW1} = 1.15 and K_{SW2} = 0.25. In other words, the system is prone to develop a SSCI when the power combinations between WFs are closer to these ratios. Thus, it can be used to evaluate the risk of undergoing a SSCI, *i.e.* if the system is stable for this worst case scenario it is stable for any other power combinations.

6.1. Numerical simulations

The dynamical behavior associated to the slices $S_{wf\mathrm{LB}}$ = 0, 0.5 and 1.5 p.u. of the stability boundary depicted in Fig. 11, is illustrated by means of numerical simulations, performing a small perturbation in the voltage at node 1008 (bulk system bus) for μ = 0.5. Three operating conditions with $S_{wf\mathrm{PM}}$ = 1 p.u. and $S_{wf\mathrm{LD}}$ = 0, 2.5 and 5 p.u., denoted by square markers in the diagrams of Fig. 11, are considered.

The results for the slice $S_{wf\mathrm{LB}}$ = 0 are shown in Fig. 12a, where the active power injected at node 10 (PMY), for the three operating conditions, is depicted. The operating points are stable, as predicted by the stability boundary diagram (Fig. 11a), and the one corresponding to $S_{wf\mathrm{LD}}$ = 2.5 p.u. presents a poor damping since it is close to the level curve (see the red marker in Fig. 11a and the red signal in Fig. 12a). The results for $S_{wf\mathrm{LB}}$ = 0.5 are depicted in Fig. 12b. The stability margin is degraded in the three cases, and the system is unstable for $S_{wf\mathrm{LD}}$ = 2.5 p.u. (condition inside the level curve for μ = 0.5 in Fig. 11b). Finally, increasing $S_{wf\mathrm{LB}}$ to 1.5 p.u., improves the stability margin and the system is stable for the three operating points (Fig. 11c).

The effect of wind turbines tripping at different WFs is illustrated by performing an additional test for μ = 0.5. The test is initialized at a stable operating point with: $S_{wf\mathrm{LD}}$ = 4 p.u. (and a wind speed v_w = 8 m/s), $S_{wf\mathrm{PM}}$ = 2 p.u. (v_w = 5.5 m/s) and $S_{wf\mathrm{LB}}$ = 0.5 p.u. (v_w = 5.5 m/s). As shown in Fig. 13a, a reduction of the wind speed at LD from 8.8 m/s to 5.5 m/s (at t = 1 s) drives the system to an unstable condition (denoted by the black triangle inside the level curve for μ = 0.5 in Fig. 11b). The SSCI triggers an oscillation of increasing amplitude that grows until

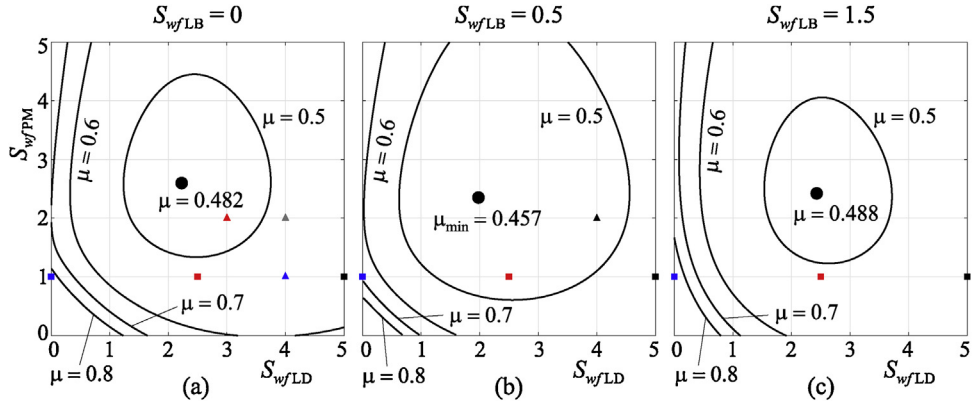

Fig. 11. Level curves in terms of μ on slices of the four-dimensional stability boundary in the plane $S_{wf\mathrm{LD}}$-$S_{wf\mathrm{PM}}$ for three different values of $S_{wf\mathrm{LB}}$. (For interpretation of the references to color in the text, the reader is referred to the web version of this article.)

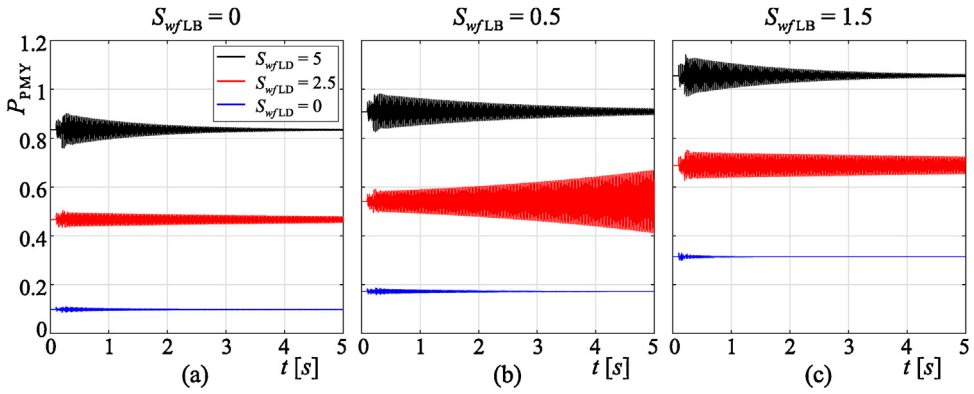

Fig. 12. Simulation of a small voltage sag at node 1008 for $\mu = 0.5$, $S_{wf\text{PM}} = 1$ p.u. and: (a) $S_{wf\text{LD}} = 0$, (b) $S_{wf\text{LD}} = 2.5$ p.u., (c) $S_{wf\text{LD}} = 5$ p.u. P_{PMY} represents the active power at the POI (node 10). (For interpretation of the references to color in the text, the reader is referred to the web version of this article.)

$t = 60$ s, where the turbines in service at LB (50 MVA) are disconnected. The new condition, with $S_{wf\text{LB}} = 0$, is stable (gray triangle in Fig. 11a), and the oscillation is damped. Nevertheless, at $t = 70$ s, a disconnection of wind turbines (100 MVA) at LD reengages the SSCI since the operating point with $S_{wf\text{LD}} = 3$ p.u. is unstable (red triangle in Fig. 11a).

The same test is repeated in Fig. 13b, but modifying the wind turbines that are disconnected at $t = 70$ s. In this case, the tripping of wind turbines (100 MVA) occurs at the WF PM instead of LD. The resulting operating condition (with $S_{wf\text{PM}} = 1$ p.u.) is stable (blue triangle in Fig. 11a) and the SSCI is not reengaged. This test reveals that the stability depends not only on the operating condition and the involved WFs, but also on the tripping sequence of wind turbines.

It is worth to mention that comparing the power ratio $K_{SW1} = S_{wf\text{PM}}/S_{wf\text{LD}}$ for the three operating conditions with $S_{wf\text{LB}} = 0$ (denoted by the triangles in the stability boundary slice of Fig. 11a), the one corresponding to the red triangle gives $K_{SW1} = 0.67$ which is closer to the worst ratio $K_{SW1} = 1.15$ than the ones corresponding to the gray triangle ($K_{SW1} = 0.50$) and the blue triangle ($K_{SW1} = 0.25$). This agrees with the simulation results, where the worst behavior (unstable) obtained for $S_{wf\text{LB}} = 0$ corresponds to the condition given by the red triangle (red portion of the simulation shown in Fig. 13a).

7. Conclusions

The analysis of a scenario with two generic WFs, revealed the main features of the stability boundary associated to the SSCI phenomenon and how it is affected by the series compensation level and the number of wind turbines in operation. An important result of this study is that the stability boundary hypersurface is convex, which is confirmed by means of numerical analysis and simulation tests performed on a case study with multiple WFs derived from a practical power system. The distribution of the power between WFs plays a decisive role, since the distance to the boundary varies, *i.e.* varying the stability margin and the damping of the subsynchronous mode. The convexity is a generic property of the stability boundary that is preserved when other key parameters such as the transmission line and collector impedances, the grid stiffness, the controllers gains or the wind speed are varied. In particular, the stability boundary surface is pulled down at (or the level curve for a given μ is displaced towards) the axis corresponding to the WF where the conditions are degraded (the electric distance to the POI is decreased, rotor control loop bandwidth is increased, or wind speed is decreased). These features can be used as a guideline to understand the behavior in systems with multiple WFs, and helps in understanding the mechanisms behind SSCI incidents reported in practical systems. In addition, the convexity of the stability boundary hypersurface, can be used to reduce the dimension of the problem by defining a worst case scenario (combinations of WFs powers) to evaluate the risk of a SSCI in a given system. Moreover, the mathematical properties of the stability boundary hypersurface (Hopf bifurcation condition) can be used to develop an algorithm to find the minimum compensation level that can trigger a SSCI incident.

Acknowledgments

This work was supported by UNS (PGI 24/K064), ANPCyT (PICT 2014-2161) and CONICET (PIP 112-20120100144).

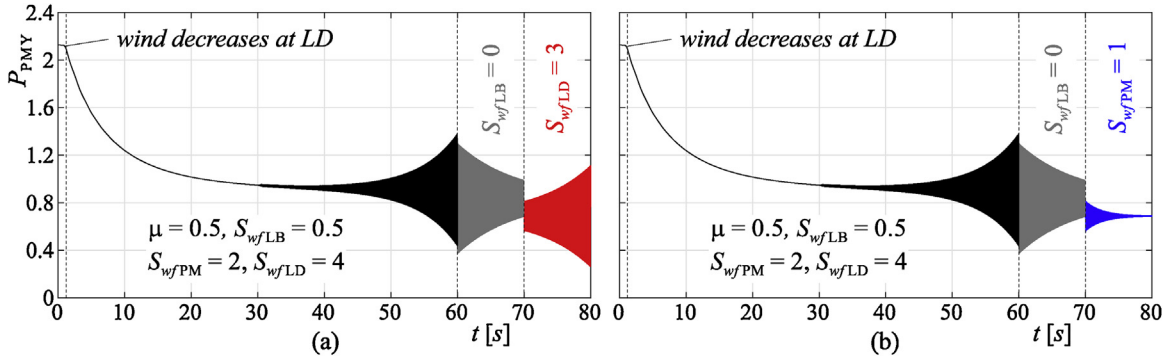

Fig. 13. Simulation of an unstable case triggered by a reduction of the wind speed in *LD*, and a successive disconnection of collectors in: (a) LB and LD, (b) LB and PM. (For interpretation of the references to color in the text, the reader is referred to the web version of this article.)

Appendix A. Description of the implemented models

In the following, the differential equations used for describing the dynamics of the WFs and transmission lines are included.

A.1 Wind farm aggregated model

The equivalent DFIG is represented in local *d-q* coordinates by the standard fourth-order model given by

$$\frac{\sigma L_r}{\omega_B}\frac{\mathrm{di_{rd}}}{\mathrm{dt}} = -v_{\mathrm{rd}} - R_r i_{\mathrm{rd}} - (\omega_s - \omega_r)\lambda_{\mathrm{rq}} - \frac{L_m}{L_s}(-v_{\mathrm{sd}} + R_s i_{\mathrm{sd}} - \omega_s \lambda_{\mathrm{sq}}), \tag{A.1}$$

$$\frac{\sigma L_r}{\omega_B}\frac{\mathrm{di_{rq}}}{\mathrm{dt}} = -v_{\mathrm{rq}} - R_r i_{\mathrm{rq}} + (\omega_s - \omega_r)\lambda_{\mathrm{rd}} - \frac{L_m}{L_s}(-v_{\mathrm{sq}} + R_s i_{\mathrm{sq}} + \omega_s \lambda_{\mathrm{sd}}), \tag{A.2}$$

$$\frac{\sigma L_s}{\omega_B}\frac{\mathrm{di_{sd}}}{\mathrm{dt}} = -v_{\mathrm{sd}} - R_s i_{\mathrm{sd}} - \omega_s \lambda_{\mathrm{sq}} + \frac{L_m}{L_r}(v_{\mathrm{rd}} + R_r i_{\mathrm{rd}} + (\omega_s - \omega_r)\lambda_{\mathrm{rq}}), \tag{A.3}$$

$$\frac{\sigma L_s}{\omega_B}\frac{\mathrm{di_{sq}}}{\mathrm{dt}} = -v_{\mathrm{sq}} - R_s i_{\mathrm{sq}} + \omega_s \lambda_{\mathrm{sd}} + \frac{L_m}{L_r}(v_{\mathrm{rq}} + R_r i_{\mathrm{rq}} - (\omega_s - \omega_r)\lambda_{\mathrm{rd}}), \tag{A.4}$$

where $\sigma = 1 - L_m^2/(L_s L_r)$, and the subindexes *r* and *s* correspond to rotor and stator quantities, respectively. The flux-current relationships are given by

$$\lambda_{\mathrm{sd}} = L_s i_{\mathrm{sd}} + L_m i_{\mathrm{rd}}, \tag{A.5}$$

$$\lambda_{\mathrm{sq}} = L_s i_{\mathrm{sq}} + L_m i_{\mathrm{rq}}, \tag{A.6}$$

$$\lambda_{\mathrm{rd}} = L_r i_{\mathrm{rd}} + L_m i_{\mathrm{sd}}, \tag{A.7}$$

$$\lambda_{\mathrm{rq}} = L_r i_{\mathrm{rq}} + L_m i_{\mathrm{sq}}. \tag{A.8}$$

The drive train of the equivalent turbine-generator is modeled by a two-mass system, with the following equations

$$\frac{d\gamma}{\mathrm{dt}} = \omega_B(\omega_t - \omega_r), \tag{A.9}$$

$$2H_t\frac{d\omega_t}{\mathrm{dt}} = T_m - K_{\mathrm{tr}}\gamma - D_{\mathrm{tr}}(\omega_t - \omega_r), \tag{A.10}$$

$$2H_r\frac{d\omega_r}{\mathrm{dt}} = -T_e + K_{\mathrm{tr}}\gamma + D_{\mathrm{tr}}(\omega_t - \omega_r), \tag{A.11}$$

where subindexes *t* and *r* correspond to turbine and generator quantities, respectively, T_m is the mechanical torque computed according to [24], and

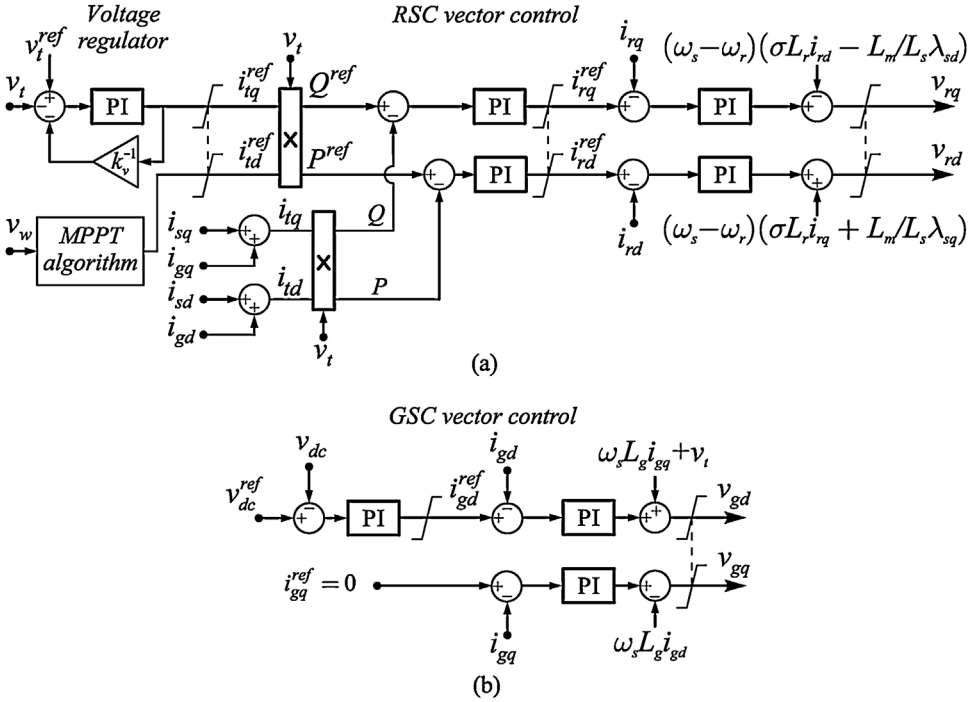

Fig. A.14. Vector control of the DFIG. PI controllers are implemented with the structure $PI(s) = K[1 + (T_i s)^{-1}]$. (a) Rotor Side Converter (RSC). (b) Grid Side Converter (GSC).

Table A.3
System parameter values.

DFIG (machine data)		LB	PM	LD
Rated power	S_N	2 MVA	2 MVA	2 MVA
Stator voltage	v_s	690 V	690 V	690 V
Number of poles	N_p	4	6	4
Stator resistance	R_s	0.00488 pu	0.00706 pu	0.0108 pu
Stator inductance	L_s	3.8451 pu	3.6710 pu	3.4640 pu
Rotor resistance	R_r	0.00549 pu	0.00500 pu	0.0121 pu
Rotor inductance	L_r	3.85234 pu	3.65600 pu	3.4720 pu
Mutual inductance	L_m	3.7528 pu	3.5000 pu	3.362 pu
Tubine inertia	H_t	4.29 s	4.00 s	4.29 s
Rotor inertia	H_r	0.9 s	0.5 s	0.9 s
Damping turbine-rotor	D_{tr}	1.5 pu	1.5 pu	1.5 pu
Stiffness turbine-rotor	K_{tr}	0.15 pu/rad	0.15 pu/rad	0.15 pu/rad

$T_e = \lambda_{sd} i_{sq} - \lambda_{sq} i_{sd}$ is the electrical torque.

The rotor voltages v_{rd} and v_{rq} are computed as denoted in the block diagram of the rotor side converter (RSC) control strategy in Fig. A.14a.

The parameters of the WFs aggregated models used in this paper are given in Table A.3.

A.2 Wind turbine control scheme

The RSC control has two internal proportional-integral (PI) loops for the rotor currents, and two external PI loops for the active and reactive power injected to the grid, respectively (see Fig. A.14a). The maximum power point tracking (MPPT) algorithm indicated is obtained from [24], where v_w is the wind speed. In addition, v_t is the magnitude of the DFIG terminal voltage.

The grid side converter (GSC) control implements two internal PI loops to set the currents, and a external PI loops to regulate the dc-link voltage (v_{dc}). The dynamics of the dc-link is represented by the first-order equation resulting from the power balance on the capacitor.

The nominal values of the controller parameters are given in Table A.4.

A.3 Transmission line models

The transmission lines are represented by π models. A generic series compensated line connecting nodes i and k is shown in Fig. A.15. The corresponding ordinary differential equations, expressed in the d–q synchronous frame with variables and parameters in p.u., are given by

$$\frac{L_{\mathrm{ik}}}{\omega_B}\frac{\mathrm{di_{ikd}}}{\mathrm{dt}} = -R_{\mathrm{ik}} i_{\mathrm{ikd}} - L_{\mathrm{ik}} i_{\mathrm{ikq}} + v_{\mathrm{id}} - v_{\mathrm{kd}} - v_{C_{\mathrm{ik\,d}}}, \tag{A.12}$$

$$\frac{L_{\mathrm{ik}}}{\omega_B}\frac{\mathrm{di_{ikq}}}{\mathrm{dt}} = -R_{\mathrm{ik}} i_{\mathrm{ikq}} + L_{\mathrm{ik}} i_{\mathrm{ikd}} + v_{\mathrm{iq}} - v_{\mathrm{kq}} - v_{C_{\mathrm{ik\,q}}}, \tag{A.13}$$

$$\frac{C_{\mathrm{ik}}}{\omega_B}\frac{\mathrm{dv}_{C_{\mathrm{ik\,d}}}}{\mathrm{dt}} = i_{\mathrm{ikd}} - C_{\mathrm{ik}} v_{C_{\mathrm{ik\,q}}}, \tag{A.14}$$

$$\frac{C_{\mathrm{ik}}}{\omega_B}\frac{\mathrm{dv}_{C_{\mathrm{ik\,q}}}}{\mathrm{dt}} = i_{\mathrm{ikq}} + C_{\mathrm{ik}} v_{C_{\mathrm{ik\,d}}}, \tag{A.15}$$

where R_{ik} and L_{ik} are the line resistance and inductance, respectively, and C_{ik} is the series capacitive compensation. For non-compensated lines, the equations reduce to

$$\frac{L_{\mathrm{ik}}}{\omega_B}\frac{\mathrm{di_{ikd}}}{\mathrm{dt}} = -R_{\mathrm{ik}} i_{\mathrm{ikd}} - L_{\mathrm{ik}} i_{\mathrm{ikq}} + v_{\mathrm{id}} - v_{\mathrm{kd}}, \tag{A.16}$$

$$\frac{L_{\mathrm{ik}}}{\omega_B}\frac{\mathrm{di_{ikq}}}{\mathrm{dt}} = -R_{\mathrm{ik}} i_{\mathrm{ikq}} + L_{\mathrm{ik}} i_{\mathrm{ikd}} + v_{\mathrm{iq}} - v_{\mathrm{kq}}. \tag{A.17}$$

Table A.4
Vector control parameters.

DFIG RSC Control (see Fig. Fig. A.14A.14a)		
Voltage droop constant	k_v	0.05
Terminal voltage PI	K_{vt} / T_{ivt}	13.5 / 3.6
External loops PI	K_e / T_{ie}	0.5 / 0.075
Internal loops PI	K_r / T_{ir}	0.025 / 0.0675
DFIG GSC Control (see Fig. Fig. A.14A.14b)		
GSC inductance	L_g	0.33 pu
dc-link capacitor	C_{dc}	10 mF
dc-link nominal voltage	v_{dc}	1200 V
dc-link PI controller	K_{vdc} / T_{ivdc}	0.35/0.2
GSC PI controllers	K_g / T_{ig}	1/0.01

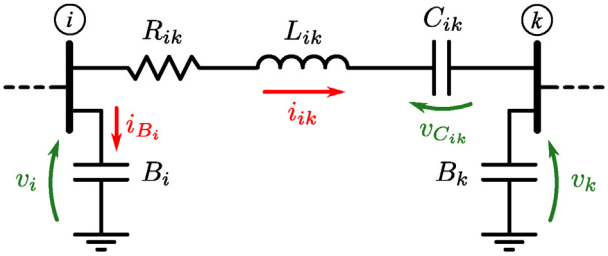

Fig. A.15. Generic π model of a series compensated transmission line.

The voltage of node i is given by

$$\frac{B_i}{\omega_B}\frac{\mathrm{dv_{id}}}{\mathrm{dt}} = i_{B_i d} - B_i v_{\mathrm{iq}}, \tag{A.18}$$

$$\frac{B_i}{\omega_B}\frac{\mathrm{dv_{iq}}}{\mathrm{dt}} = i_{B_i q} + B_i v_{\mathrm{id}}, \tag{A.19}$$

where B_i is the charging susceptance, and i_{B_i} is the algebraic sum of the currents at node i.

References

[1] G.D. Irwin, A.K. Jindal, A.L. Isaacs, Sub-Synchronous control interactions between Type 3 wind turbines and series compensated AC transmission systems, IEEE PES General Meeting, Detroit, USA, 2011, pp. 1–6.

[2] L. Fan, C. Zhu, Z. Miao, M. Hu, Modal analysis of a DFIG-based wind farm interfaced with a series compensated network, IEEE Trans. Energy Convers. 26 (4) (2011) 1010–1020.

[3] Z. Miao, Impedance-model-based SSR analysis for type 3 wind generator and series-compensated network, IEEE Trans. Energy Convers. 27 (984–991) (2012) 4.

[4] B. Badrzadeh, M. Sahni, Y. Zhou, D. Muthumuni, A. Gole, General methodology for analysis of sub-synchronous interaction in wind power plants, IEEE Trans. Power Syst. 28 (2) (2013) 1858–1869.

[5] L. Fan, Z. Miao, Mitigating SSR using DFIG-based wind generation, IEEE Trans. Sustain. Energy 3 (3) (2012) 349–358.

[6] H. Mohammadpour, E. Santi, SSR damping controller design and optimal placement in rotor-side and grid-side converters of series-compensated DFIG-based wind farm, IEEE Trans. Sustain. Energy 6 (2) (2015) 388–399.

[7] A.E. León, J.A. Solsona, Sub-synchronous interaction damping control for DFIG wind turbines, IEEE Trans. Power Syst. 30 (1) (2015) 419–428.

[8] V. Virulkar, G. Gotmare, Sub-synchronous resonance in series compensatedwind farm: a review, Renew. Sustain. Energy Rev. 55 (2016) 1010–1029.

[9] L. Gross, Sub-synchronous grid conditions: new event, new problem, and new solutions, 37th Annual Western Protective Relay Conference, Spokane, Washington, USA, 2010, pp. 1–19.

[10] K. Narendra, D. Fedirchuk, R. Midence, N. Zhang, A. Mulawarman, P. Mysore, V. Sood, New microprocessor based relay to monitor and protect power systems against sub-harmonics, IEEE Electr. Power and Energy Conf. Winnipeg, Canada, 2011, pp. 438–443.

[11] Y.-H. Wan, Synchronized Phasor Data for Analyzing Wind Power Plant Dynamic Behavior and Model Validation, Tech. Rep. NREL TP-5500-57342, NREL, Golden, Colorado, 2013.

[12] L. Wang, X. Xie, Q. Jiang, H. Liu, Y. Li, H. Liu, Investigation of SSR in practical DFIG-based wind farms connected to a series-compensated power system, IEEE Trans. Power Syst. 30 (5) (2015) 2772–2779.

[13] M. Wu, L. Xie, L. Cheng, R. Sun, A study on the impact of wind farm spatial distribution on power system sub-synchronous oscillations, IEEE Trans. Power Syst. 31 (3) (2016) 2154–2162.

[14] X. Xie, X. Zhang, H. Liu, H. Liu, Y. Li, C. Zhang, Characteristic analysis of sub-synchronous resonance in practical wind farms connected to series-compensated transmissions, IEEE Trans. Energy Convers. 32 (3) (2017) 1117–1126.

[15] A.E. León, G. Revel, D.M. Alonso, G. Alonso, Wind power converters improving the power system stability, IET Generation, Transm. Distrib. 10 (7) (2016) 1622–1633.

[16] A.E. León, Integration of DFIG-based wind farms into series-compensated transmission systems, IEEE Trans. Sustain. Energy 7 (2) (2016) 451–460.

[17] A.E. León, Short-term frequency regulation and inertia emulation using an mmc-based mtdc system, IEEE Trans. Power Syst. 33 (3) (2018) 2854–2863.

[18] G. Revel, A.E. León, D.M. Alonso, J.L. Moiola, Multi-parameter bifurcation analysis of subsynchronous interactions in DFIG-based wind farms, Electr. Power Syst. Res. 140 (2016) 643–652.

[19] H. Liu, X. Xie, C. Zhang, Y. Li, H. Liu, Y. Hu, Quantitative SSR analysis of series-compensated DFIG-based wind farms using aggregated RLC circuit model, IEEE Trans. Power Syst. 32 (1) (2017) 474–483.

[20] E. Muljadi, S. Pasupulati, A. Ellis, D. Kosterov, Method of equivalencing for a large wind power plant with multiple turbine representation, IEEE PES General Meeting, Pittsburgh, USA, 2008, pp. 1–9.

[21] Y.A. Kuznetsov, Elements of Applied Bifurcation Theory, 3rd ed., (2004) New York.

[22] A. Dhooge, W. Govaerts, Y.A. Kuznetsov, H. Meijer, B. Sautois, New features of the software MatCont for bifurcation analysis of dynamical systems, Math. Comput. Model. Dyn. Syst. 14 (2) (2008) 147–171.

[23] L. Yang, Z. Xu, J. Østergaard, Z.Y. Dong, K.P. Wong, X. Ma, Oscillatory stability and eigenvalue sensitivity analysis of a dfig wind turbine system, IEEE Trans. Energy Convers. 26 (1) (2011) 328–339, https://doi.org/10.1109/TEC.2010.2091130.

[24] J.G. Slootweg, S.W.H. De Haan, H. Polinder, W.L. Kling, General model for representing variable speed wind turbines in power system dynamics simulations, IEEE Trans. Power Syst. 18 (1) (2003) 144–151.